ETH
Eidgenössische Technische Hochschule Zürich
Swiss Federal Institute of Technology Zurich

Empa
Materials Science and Technology

Willy Gächter

Experimental and numerical sensitivity analysis of melt pool dimensions for LPBF Hastelloy X

Bachelor's thesis

Institute of Mechanical Systems
Swiss Federal Institute of Technology (ETH) Zurich

Advisors

Prof. Dr. E. Mazza, Dr. E. Hosseini, Mr. J. Tang

Institute of Mechanical Systems, ETH Zürich
Experimental Continuum Mechanics, Empa

July 8, 2022

Abstract

Laser powder bed fusion (LPBF) is an additive manufacturing (AM) method enabling the production of highly complex parts that cannot be produced using conventional manufacturing methods. Improving the quality of LPBF parts and hence their extensive employment in industry, particularly for critical applications, require a better understanding of the sensitivity of different product characteristics to the LPBF process parameter and therefore adopting optimized process conditions accordingly.
This study aims to analyze the sensitivity of the formed melt pool dimensions for LPBF Hastelloy X to process parameters such as laser power, scan speed, laser energy density and printing position. Experimental data from 90 samples, printed with different LPBF process conditions, were carefully assessed to understand the sensitivity of melt pool depth, width and area to the process parameters. As a result, it came to the light that melt pool depth is more sensitive to a change in the process conditions than the other parameters. Additionally, it was found that, among the examined process parameters, the laser energy density was the most dominant factor in determining the dimensions of the melt pool.
The experimental observations were then exploited to develop a representative thermal model within the Abaqus finite element (FE) package to simulate the LPBF process. The main focus was on calibrating the parameters of the Goldak heat source model to provide exemplary melt pool dimension predictions. It was concluded that it is impossible to derive a unique set of Goldak parameters that enables the FE model to reliably represent the melt pool dimensions for different process conditions. It has been shown that considering Goldak parameter b as a linear function of the energy density leads to significantly improved consistency of numerically calculated and experimentally measured melt pool dimensions. However, it should be noted that since the developed FE model is a simplified representation of the actual process and does not consider several phenomena such as melt pool flow, material evaporation, and the complex laser absorption/reflection path, some levels of deviation between simulation and experimental results remains.

Acknowledgment

First of all, I want to thank Prof. Dr. E. Mazza for making it possible for students of ETHZ to write their thesis at EMPA in the HTIG and for having put together such an extraordinary team there.
Many thanks to Dr. E. Hosseini for offering such an interesting project, organizing the entry into EMPA and always being there when an urgent problem needed to be solved. I am very thankful for the weekly meeting which made it possible to discuss problems and further proceedings as well as receiving precious inputs and thoughtful opinions to ongoing results.
Sincere thanks to Mr. J. Tang for always being available and reacting rapidly to obstacles, putting heads together to delve into problems more detailed and proposing further approaches how to advance in the project. Special thanks for delivering the images of the experimental part in this thesis and for handing out all the material to have a quick entry into the subject at the beginning. Much gratitude for assisting in the installation and use of all the software, scripts and code to work on the project and run the Simulations properly.

Contents

1. Introduction

1.1. Laser Powder bed fusion

LPBF is a manufacturing method in the group of Additive manufacturing where a part is built up on a build plate by adding material while subtractive manufacturing methods grind a raw material block until the desired shape is obtained. There are many different ways of AM with a big variety of materials and distinct ways of converting the material from its raw state to a finished part but all of them work in the same fashion [1]. Not only the efficient use of material is an advantage compared to conventional manufacturing also the high level of possible part complexity makes it attractive to achieve higher levels of performance in the application. The use in testing and prototyping is another gain of AM as no additional tools are needed [2]. This is achieved by building in a layer by layer manner and only adding material at the position where it is needed [3]. Although there is less waste, the process is very time consuming. Usually, in AM the part is built up from a 3D-model converted to an STL file, this model is then divided into layers with the desired printing layer thickness. The AM-machine continues with depositing the layers one over another which finally results in a finished part where in some cases post processing is necessary [1]. Post processing can be dependent on the material used and on the purpose of the finished part. For example in metal additive manufacturing (MAM) it is desirable to get rid of sharp edges or notches due to high stresses and fatigue cracks forming there. In most AM methods it is also needed to additionally build support material with different purposes that needs to be removed afterwards [3].
In a Laser powder bed fusion machine the main process is done on a vertically movable build plate (Fig. 1.1). The raw material is delivered in powder form which is melted trough a laser heat source during the scan procedure. After the melt pool cools down it solidifies and leaves a single layer of material for the resultant part. In the next step the powder delivery platform illustrated in the left part of Fig. 1.1 with the material reserve is raised leaving excess powder over the process table where a coater picks it up and fills the cavity of the main plate with it. Now to create the first layer, a mirror is redirecting the laser over the area where bulk material is needed for the final part, thus melting the powder and leaving a track of bulk material after cool down. For the first layer the material is directly connected to the build plate in some cases while additional spots are melted to form the support material needed for future overhang features. This is essential as during the process the connection to the build plate ensures that the heat is conducted away [5]. Further important is the laminar gas flow of an insulating and neutral gas like Argon or Nitrogen that prevents the highly reactive melt pool from oxidation or other bad influences [6]. After the laser has finished its full track, the build plate is lowered again and the whole process repeats until the full part is finished. For

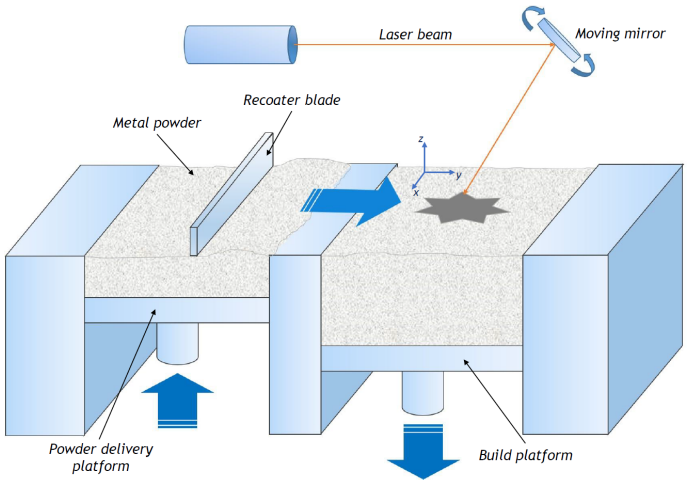

Figure 1.1.: Illustration of a LPBF process environment denoted with its fundamental elements [4].

the laser it is desirable to have full control over the scan speed and the power which is not always feasible as the laser is redirected by a moving mirror with a certain mass and inertia. During the printing process there is always a possibility of defects in the layers. One of the defects usually occurring at lower energy densities is lack of fusion where the powder is not melted trough the full layer thickness resulting in a not fully connected track. The line energy density(LED) is a common measure for the energy input, calculated by dividing laser power trough scan speed. For high energy input the laser does not only melt the material in the melt pool but also evaporates the metal around the center of the laser creating a hole trough the pressure triggered by the higher volume of metal vapor. The laser is being reflected inside this so called keyhole and even more energy is absorbed leading to a deeper melt pool until an equilibrium between surface tension of the melt pool and the vapor pressure is reached. This keyhole moves together with the laser in the scan direction and can collapse spontaneously where it is possible that a part of the vaporized metal cannot escape the hole in time before the melt pool solidifies . This means that the vapor gets trapped leaving behind a pressurized spherical pore in the material having a bad influence on the mechanical properties of the final part. The higher the energy input the deeper the resulting keyhole and the higher the probability that a pore is left behind [7]. Another unwanted effect in LPBF that occurs during the production of a part are residual stresses caused trough thermal gradients which can result in the distortion of the final product. Most of these unwanted effects still need further research to have full control over the manufacturing process and receive flawless parts. In this project the emphasis lies on the different trends of the printing parameters such as the laser power, the scan speed and the effect of the printing direction or position.

1.2. Simulation principle and Goldak heat source model

A common tool to predict physical properties of a part before producing it is the use of a simulation software that is able to calculate the outcome with a certain precision. One of the methods to do so is the Finite element analysis (FEA) which is able to solve a problem numerically by dividing a structure into smaller substructures that allow it to use simplified equations. Abaqus Simulia is a well known FEA software and is being used in this project together with its AM modeler plug-in where the simulation of an AM process is simplified. The usual process in the simulation is divided into different steps where processes like applying a powder layer or moving a laser heat source can be defined and executed. The heat source model used in this project is the Goldak heat source as implemented in Abaqus illustrated in Fig. 1.2. The scan direction is in the x-direction of the shown coordinate system.

$$q = q_f \; when \; x \geq 0$$
$$= q_r \; when \; x < 0$$

$$q_{f/r} = \frac{6\sqrt{3} f_{f/r} Q}{abc\pi\sqrt{\pi}} e^{(-\frac{3x^2}{c_{f/r}^2})} e^{(-\frac{3y^2}{a^2})} e^{(-\frac{3z^2}{b^2})}$$

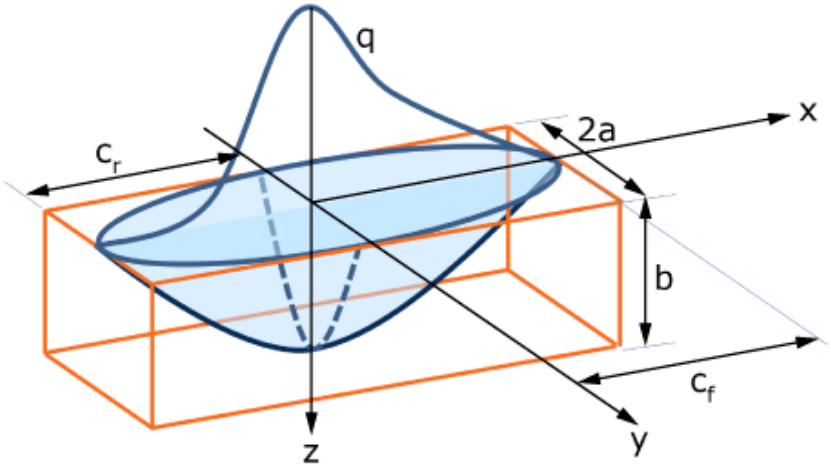

Figure 1.2.: Goldak heat source model with its distribution and the relevant parameters used by the AM modeler in Abaqus [8].

In this project only four of the parameters involved are observed as well as the absorptivity. The Goldak parameter a determines the width of the heat source while b changes the depth. To adjust the distortion in the front part the parameter c_f can be changed while c_r sets the elongation of the heat source in the rear direction. All the Goldak parameters are defined in mm while the absorptivity is given as a decimal describing the percentage of energy absorbed. The remaining two, f_f and f_r are controlling the box

size of the model but in this project they are left at the default value of 1.
The simulation can be used to avoid the earlier mentioned defects like the deformation trough residual stresses in the post processing, lack of fusion or keyhole pores. This is much less expensive than the method of trial and error making it very attractive to have a precise simulation. But to predict the temperature distribution during a printing job using numerical methods, the model used needs to be validated and examined to its limitations first. Therefore the sensitivity of the Goldak parameters is analyzed and later in this project the gathered data from the experiment is used to calibrate the dimensions of the Goldak heat source.

2. Methodology

2.1. Experiment

The goal in this project is to examine the sensitivity of the melt pool width and depth as well as the cross sectional melt pool area to a change in the printing parameters of the laser power, scan speed and the printing position. Therefore an experiment is designed in a way such that all these properties can be analyzed for different conditions listed in Tab. 2.1. This means to achieve the most experimental output with only one time performing the experiment. The first thought is to print single layer tracks on a single printing surface (Fig. 2.1) made out of Hastelloy X [9] with changing laser power and scan speed for each track and repeating this process multiple times to receive different samples for the same conditions. The machine used for the printing job is a Sisma mysint 100 from SISMA S.p.A., Italy. This setup can be more effective by examining different

Figure 2.1.: Main plate for the LPBF process made of Hastelloy X.

layer thicknesses of powder at the same time. This is done by machining cavities into the surface of the base plate with varying depths of $20, 30$ and $40\mu m$ as seen in the sketched setup in Fig.2.2. The surface roughness of the unique printing plate is chosen as low as possible with an $Ra - value$ of 0.02 as in similar experiments like the one from Keshavarzkermani the plate had height differences higher than the actual layer thickness [10]. At the beginning of the printing job the cavity is filled with Hastelloy X powder of $30\mu m$ average grain size, then the laser with a spot size of $55\mu m$ will scan over the track multiple times until five samples are created for each printing condition according to the draft in Fig. 2.3.
To measure the melt pool dimensions of each track, the base plate with the finished single tracks on top is cut into pieces perpendicular to the scan direction at the eight positions with the different layer thickness in the first half and the second half of the tracks. The

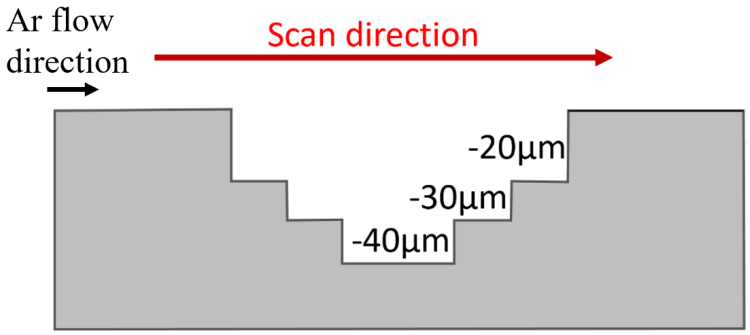

Figure 2.2.: Sketched cross section along the scan direction of the base plate used in the experiment.

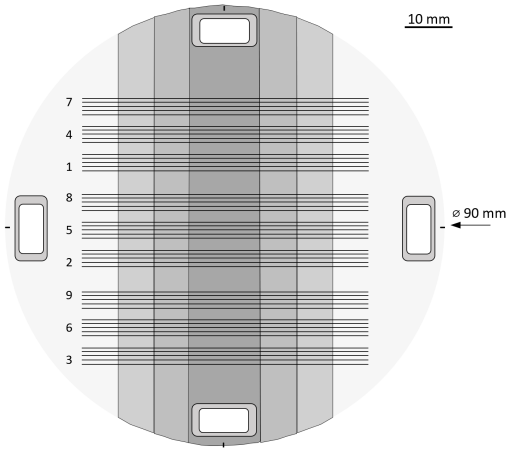

Figure 2.3.: Draft of the base plate with the single tracks and the respective number of the printing condition used from Tab. 2.1.

Pr. cond. [#]	Laser Power [W]	Scan speed [$\frac{mm}{s}$]	estimated LED [$\frac{J}{mm}$]	calculated LED [$\frac{J}{mm}$]
1	125	550	0.222 ± 0.005	0.227
2	125	700	0.185 ± 0.008	0.179
3	125	800	0.154 ± 0.003	0.156
4	175	800	0.222 ± 0.005	0.219
5	175	900	0.185 ± 0.008	0.194
6	175	1150	0.154 ± 0.003	0.152
7	200	900	0.222 ± 0.005	0.222
8	200	1100	0.185 ± 0.008	0.182
9	200	1300	0.154 ± 0.003	0.154

Table 2.1.: Experimental printing conditions with the estimated LED used to compare the experimental results in more or less the same LED ranges.

first half is distinguished from the second half by having the sequence of layer thickness in ascending and descending order. After grinding and polishing the surfaces of the obtained cross sections with SiC grinding papers together with 3, 1 and 0.05 μm SiC polishing suspension, the samples are etched with a Glyceregia reagent for 2 min. This process is done to receive a flawless surface of the samples such that the melt pool can be recognized under a scanning electron microscope. To take images of the melt pool a FEI Quanta 650 SEM is used and greyscale images are saved electronically. Further, the images are then processed by a self-made Matlab code where the melt pool is selectively cut out. At the same time, all dimensions are measured automatically and saved in a Excel spreadsheet. The definitions of the dimensions are uniform for every melt pool such that the dimensions remain meaningful (Fig. 2.4). The melt pool shapes can be extraordinary under some conditions by leaving excess material from the bead on top to the sides left or right of the melt pool influencing the measured width. For this the width is defined as the distance between the edges of the melted base plate as marked in Fig. 2.4a to reduce the influence of spattering on the surface. The depth is also defined in a way to make it independent of the varying shapes of the bead by starting to measure the depth at the height of the base plate surface down into the material to the lowest point of the once molten material. The third dimension observed in this project is the cross-sectional area of the melt pool. As the area is highly dependent on the width and depth it will only be used for the calibration of the simulation later on. There the bead will not be simulated so that in the experiment only the area below the main plate surface will be extracted as shown in Fig. 2.4b.

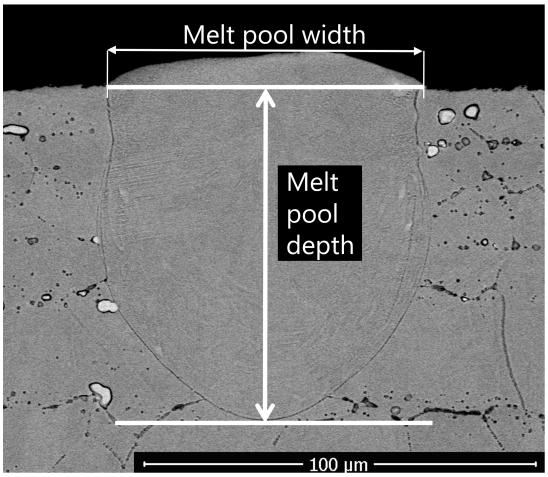

(a) Dimensions of depth and width shown on a SEM image of a melt pool section.

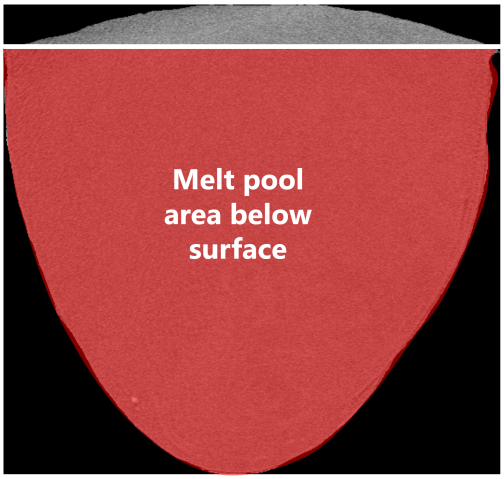

(b) A Cut out melt pool after processing with the Matlab tool showing the measured area of the melt pool illustrated as the read area. The white line on top highlights the original position of the surface from the printing plate.

Figure 2.4.: Melt pool images demonstrating the definitions of the dimensions.

2.2. Simulation setup

In the simulation part of this project the focus lies on the calibration of the simulation on the basis of the gathered experimental data. The ultimate goal is the determination of the temperature distribution during the printing process which could help in future cases for predicting thermo-mechanical phenomenons. From the previous portrayed experimental setup the positions without powder are chosen for simplicity as it is imaginable that the powder can be modeled using a different absorptivity and thermal conductivity making the calibration more complicated. To obtain a heat profile close to the experimental one it should also deliver correct results for a single track scan without powder added on the main plate. To start the adjustment of the Goldak heat source parameters in the simulation, first the sensitivities of the five chosen parameters presented in Chapter 1 Introduction are examined. This is done by simulating a 1.5 mm single-track Abaqus AM-modeler job. The setup consists of an adapted base plate model created by P. Gh. Ghanbari with a finer mesh size in the region around the track shown in Fig. 2.5. For the

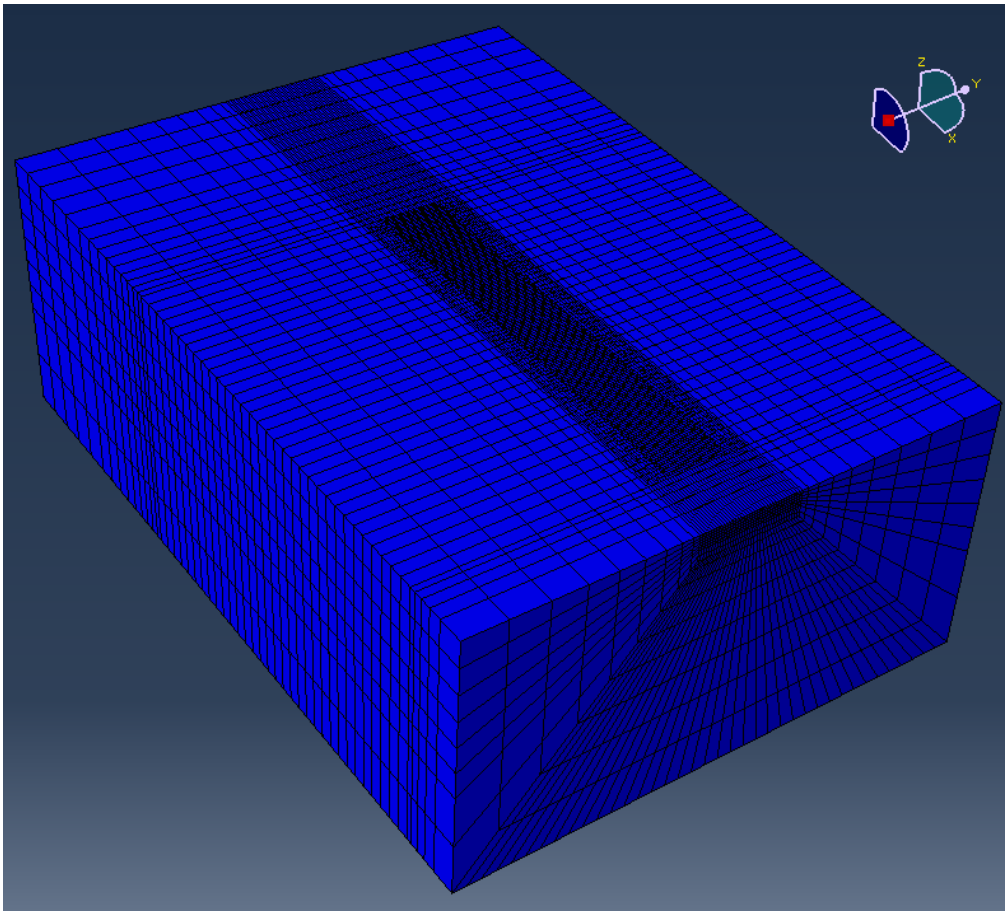

Figure 2.5.: Base plate model used in the simulation with an adapted mesh for the 1.5mm single-track simulation.

material properties the values shown in Tab. 2.2 are used. There it can be seen that the Density is held constant over all temperatures to keep the computation more simplified. The conductivity and the specific heat have two temperature dependent values defined. For changing temperature they are linearly inter- and extrapolated by Abaqus to adapt the properties during the computation.

Density $\frac{kg}{mm^3}$	Conductivity $[\frac{W}{mmK}]$	Temp $[°C]$	Spec. Heat $[\frac{J}{kgK}]$	Temp $[°C]$
8.22E-06	0.0092	25	486	25
8.22E-06	0.034	1260	784	1000

Table 2.2.: Material properties used in the simulation for the build plate of Hastelloy X.

Subdiv x	Subdiv y	Subdiv z	ff	fr	Box size
20	20	20	1	1	1

Table 2.3.: Values for the remaining Goldak parameters that are held constant.

The remaining Goldak parameter needed in Abaqus are shown in Tab. 2.3 which are held constant for the whole project. Finally the dimensions are extracted from the created *.dat* file using a Matlab tool. In the *.dat* file each node is saved with its respective temperature during each step of the simulation. From this information the border of the melt pool is found with a linear interpolation of the temperature where a region counts as melted when it reaches a temperature over $1307°C$ which is the middle point between solidus and liquidus line from Hastelloy X found in the manual [9]. The dimensions are then extracted from the so obtained body in the simulation. To find the sensitivity of Goldak a, b, cf, cr and the *absorptivity* initial values for the parameters are set around their corresponding experimental data and settings from literature. The sensitivity is once observed by varying each parameter in a small range around the initial setting and observing the effect on the dimensions. To have an overview for different printing conditions three more conditions are chosen and once simulated with the same initial parameters for all conditions and increasing each parameter by 10% while the others are kept constant to see the percentage change in the dimensions. Finally to calibrate the heat source an attempt with constant Goldak parameters for every condition is foreseen and the further approach is dependent on the outcome of the sensitivity part beforehand.

3. Results and Discussion

3.1. Experimental Results

The results from the experiment are collected in a spreadsheet by the self-made Matlab tool (mentioned in chapter 2 Methodology) extracting them. For the analysis of them they are illustrated in different plots and compositions. The data with the least deviations are the ones from the beginning of the track without powder, for this reason these values are used to discuss the general trend and sensitivity of the dimensions to the printing parameters. As earlier mentioned the trend of the area will not be examined as it is dependent on both width and depth but the aspect ratio of depth divided by width will be analyzed as it is used as a measure for the melting mode of the melt pool [11]. The plots of the experimental results were drawn by J. Tang as well as some explanations of the trends stem originally from him.

3.1.1. Effect of laser power and scan speed

The two main parameters that are tuned in the LPBF process are the laser power(LP) and the scan speed. To analyze the effect of them onto the melt pool dimensions the width, depth (Fig. 3.1) and the depth/width-ratio (Fig. 3.2) are plotted onto the scan speed. In Fig. 3.1 on the left the influence of the scan speed on the melt pool depth can

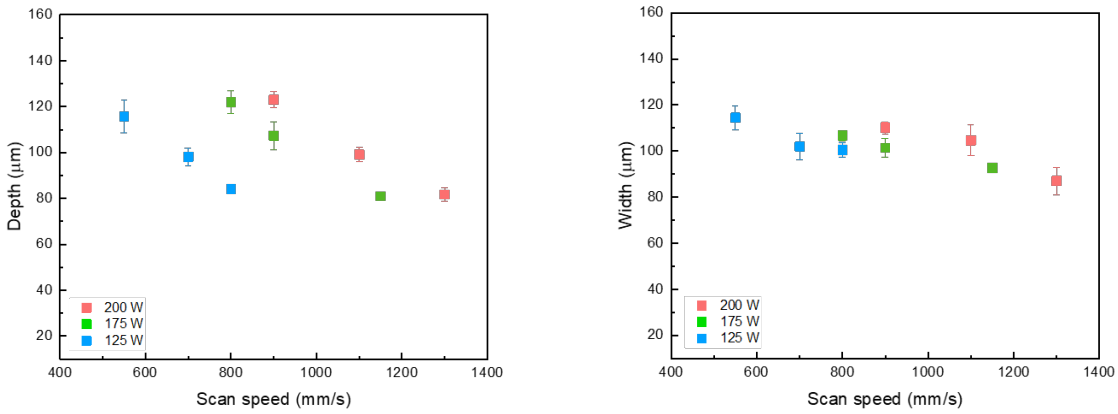

Figure 3.1.: Experimental results for the melt pool depth and width at the beginning of the track in the y-axis plotted on the scan speed in the horizontal axis. The laser power is illustrated in different colors.

be seen. Illustrated as the same color for a constant laser power, the depth is decreasing a lot. On the right side the width shows a decreasing trend as well but not as steep as for the depth. For the depth/width ratio in Fig. 3.2 the trend is also decreasing but most important in the depth/width ratio it is shown that all printing conditions are under keyhole mode at the beginning of the track as the ratio is higher than 0.5 for all results [11]. For the effect of the laser power one needs to take a look at two conditions with

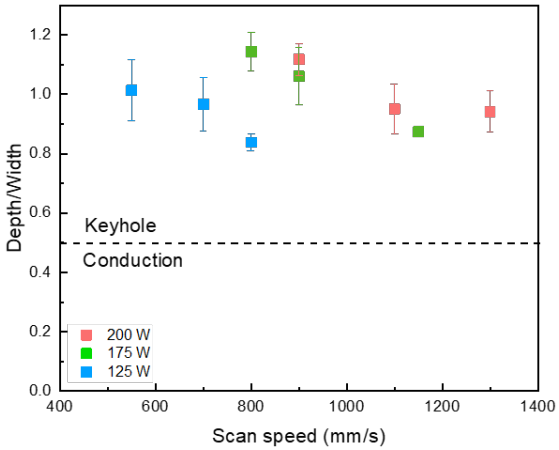

Figure 3.2.: The calculated depth/width-ratio in the vertical axis drawn onto the respective scan speed on the horizontal axis. Additionally the border for the distinction of keyhole and conduction mode drawn in at a ratio of 0.5 given from literature [11].

the same scan speed like the ones with 800 and 900$\frac{mm}{s}$, there once again the depth is increasing more for a higher laser power than the width but both of them are increased. Here it is clear that a higher laser power provides a larger energy input into the system leading to a growth in all dimensions.

3.1.2. Effect of Line energy density

To analyze the influence of the one dimensional energy input, plots with the energy density in the horizontal axis are observed. In this case one would expect that the dimensions are again increasing for a higher energy density which can be seen in the two plots for the depth and width Fig. 3.3.
This time the trend of both depth and width seems to be linear to the LED. The value with the highest energy density is a little bit out of line in the depth plot while the width is fluctuating in the lower energy densities. In Fig. 3.4 of the depth/width-ratio, the deviations of the marginal values remains but so does the general trend of increase over the growing energy density. This shows that the LED can roughly be used to increase the dimensions as already expected.

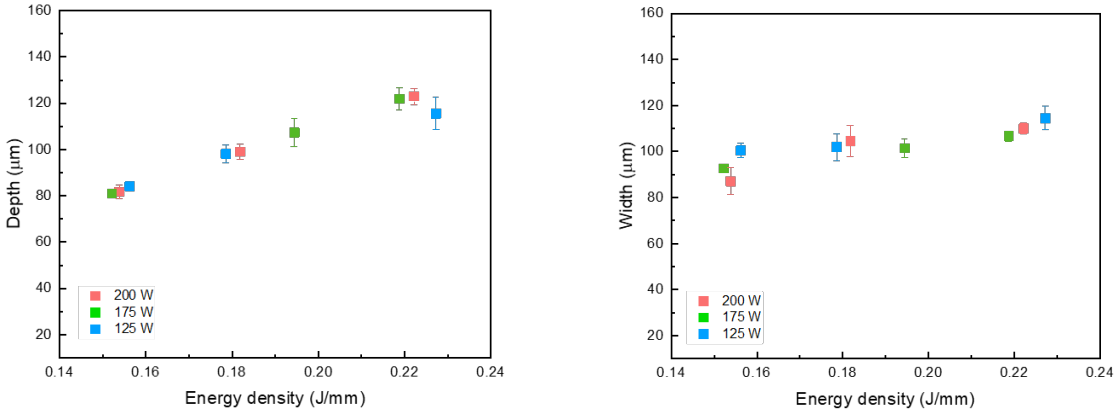

Figure 3.3.: Experimental width and depth from the beginning of the track presented in dependence of the LED.

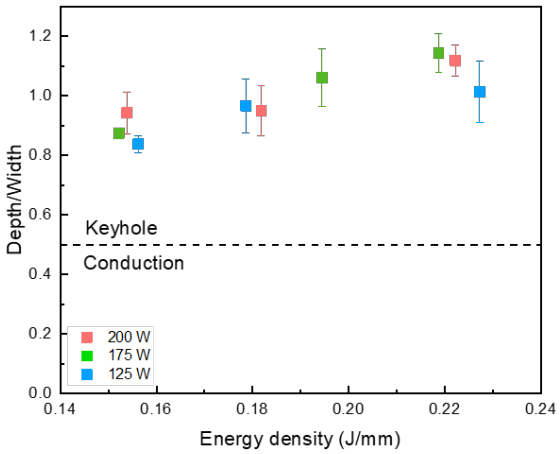

Figure 3.4.: Depth/width-ratio plotted on the energy density.

3.1.3. Effect of printing position

The last influence that is observed is the effect of the printing position. For this not only the results at the beginning of the track are shown but also the ones from the end of the track without powder layer. For the plots again the scan speed is plotted on the horizontal axis and the different laser powers are shown in different color (Fig. 3.5,3.6) while the results from the end of the track are illustrated as empty symbols and the ones from the beginning are filled like before. On the plot of the depth and the one of the depth/width-ratio, in all cases except the one with the lowest scan speed, the result from the end of the track is lower than the one from the beginning. The same applies for the width just with the opposite trend so the data at the beginning of the track is lower as the one from the end. This behavior can be an influence of the plume built up above the melt pool where the interaction of the laser with this nanoparticles ejected

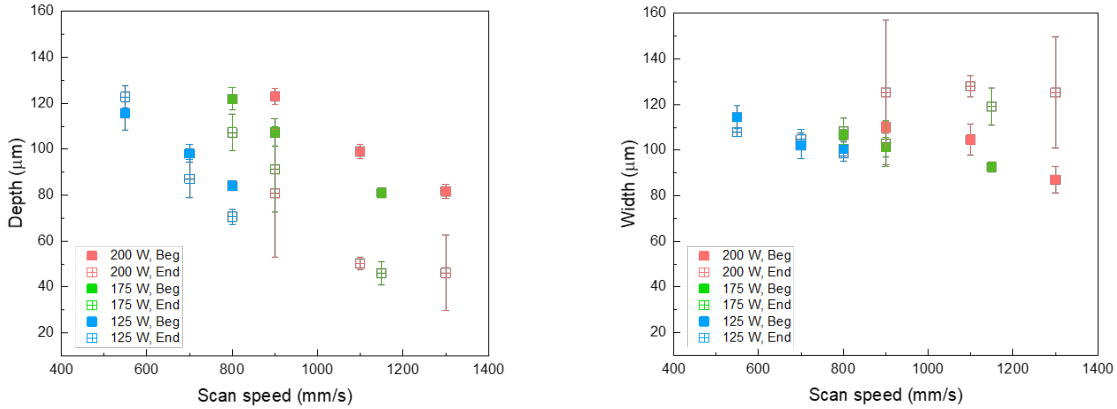

Figure 3.5.: The results for depth and width in dependence of the scan speed and distinguished between laser power as well as designated as from the beginning or end of the track

from the melt pool can cause beam attenuation trough scattering the laser or absorbing a fraction of the laser energy [12]. This effect is dependent on the laser position and scan speed, but in this project it is not intended to delve deeper into this subject. The behavior is better explained in Zheng 2018 [13]. With the effects of the plume the larger deviation ranges for higher laser power or scan speed can be explained as the scattering of the laser is intensified in these cases.

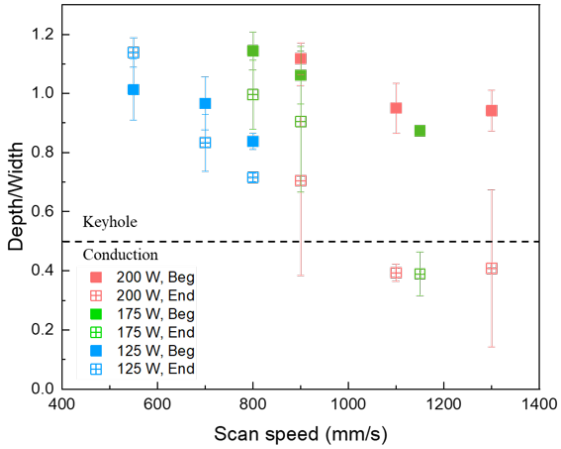

Figure 3.6.: Depth/width-ratio for all conditions with 0 μ m layer thickness plotted on the scan speed.

3.2. Simulation parameters

3.2.1. Sensitivity of Goldak parameters

Before the Goldak heat source is calibrated with the experimental data the behavior of each parameter is examined. For this purpose the printing condition number 2 from Tab. 2.1 was chosen in a first trial to see the effects of change in a Goldak parameter onto the melt pool dimensions in the simulation. For the initial values of the simulation parameters a was set to approximately half the melt pool width extracted from the experiment while b was chosen a little more than the depth of the experiment. cf is chosen equal and cr a little more than a. From Irwin 2021 it is proposed to use an absorptivity of 0.8 for conditions in keyhole mode but to keep the $absorptivity(abs)$ low a value of 0.75 was first used [14]. This served only as a first overview over the sensitivity in the simulation therefore it is not further analyzed but the effect on the dimensions of the simulated melt pool can be seen in Fig. A.2. For the second step more conditions are added to the simulations where the same initial parameter setting was used and then in a second simulation increased by 10% to see the effect onto the simulated melt pool dimensions. Illustrated in Fig. 3.7,3.8 and 3.9 the percentage change of the three important dimensions is shown in dependence of a 10% increase of each Goldak parameter one after another.

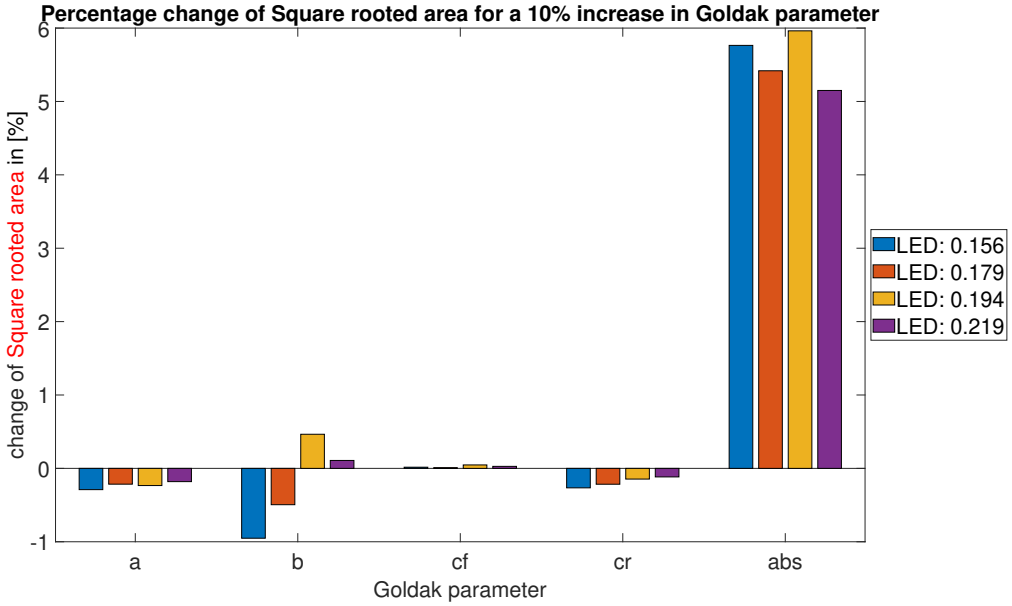

Figure 3.7.: Change of the melt pool square rooted area shown in percent for a 10% change in each Goldak parameter while the other parameters are kept constant.

The abs has clearly an increasing effect on all dimensions while the effect is the highest for the width so that a higher energy input increases the width more than the depth. Also very clear is the negligible influence of cf which has the lowest effect on all dimensions.

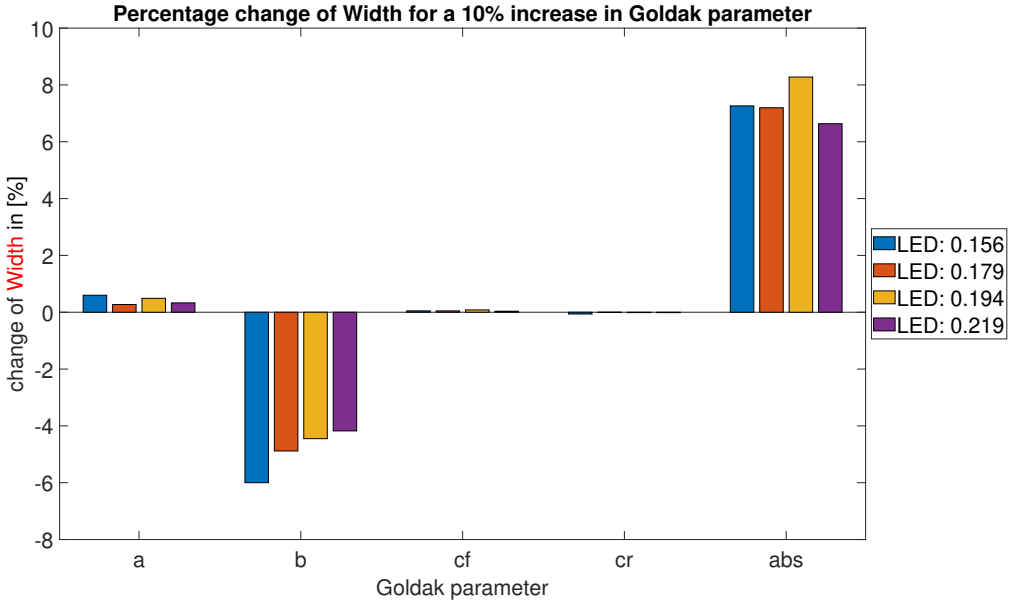

Figure 3.8.: Change of the melt pool width shown in percent for a 10% change in each Goldak parameter while the other parameters are kept constant.

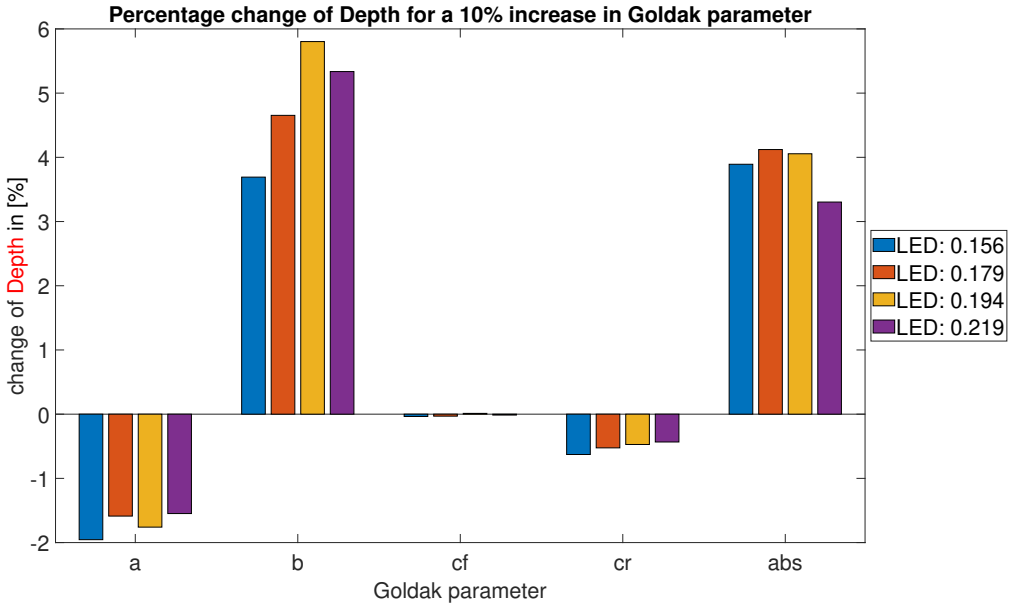

Figure 3.9.: Change of the melt pool depth shown in percent for a 10% change in each Goldak parameter while the other parameters are kept constant.

cr has a decreasing behavior for the depth (Fig. 3.9) and practically no influence in the width (Fig. 3.8) hence it is reducing the area (Fig. 3.7). *a* and *b* have more or less the opposing behavior in regard of the depth and width where each of them increases the

corresponding dimension to their Goldak direction and mostly decreases the area but the effect of a is smaller than the influence of b. To change the melt pool shape now one can see that the parameters a and b can be used.

3.2.2. Calibration of the simulation

In the last part of this project the gathered experimental data is used for adjusting the Goldak heat source to approximate the real temperature distribution during the printing job with the simulation. This is done by using the melt pool dimensions as a guideline for the heat source because the prediction of the melt pool dimensions in the simulation should get close to the experimental ones as soon as the temperature profile gets closer to the real one. In the first try the previously used parameters shown in Tab. 3.1 from the sensitivity analysis are expanded and used for all conditions as the condition with P: 125 and Energy density (E): 0.179 had already close values to the ones from the experiment.

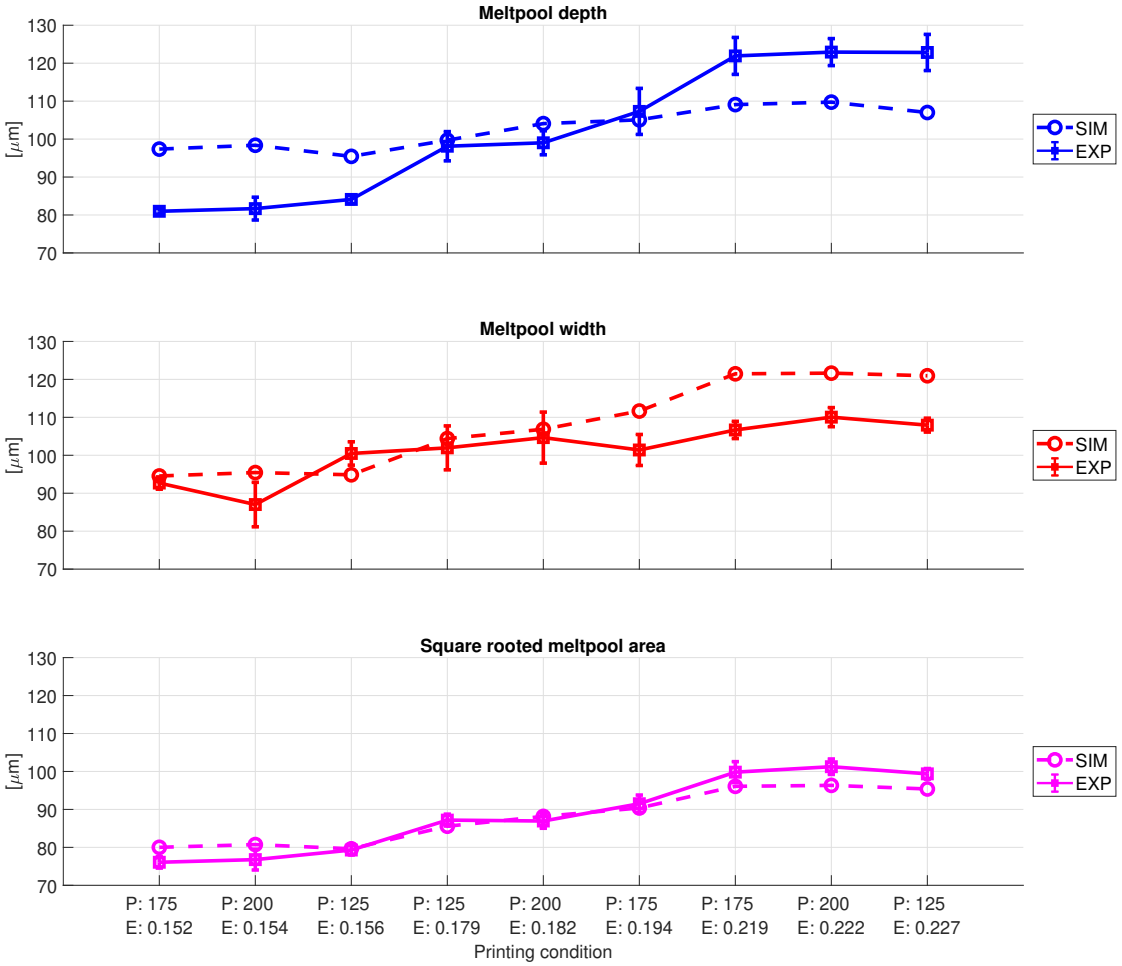

Figure 3.10.: The simulation melt pool dimensions compared to the experimental dimensions with constant Goldak parameters for each printing condition.

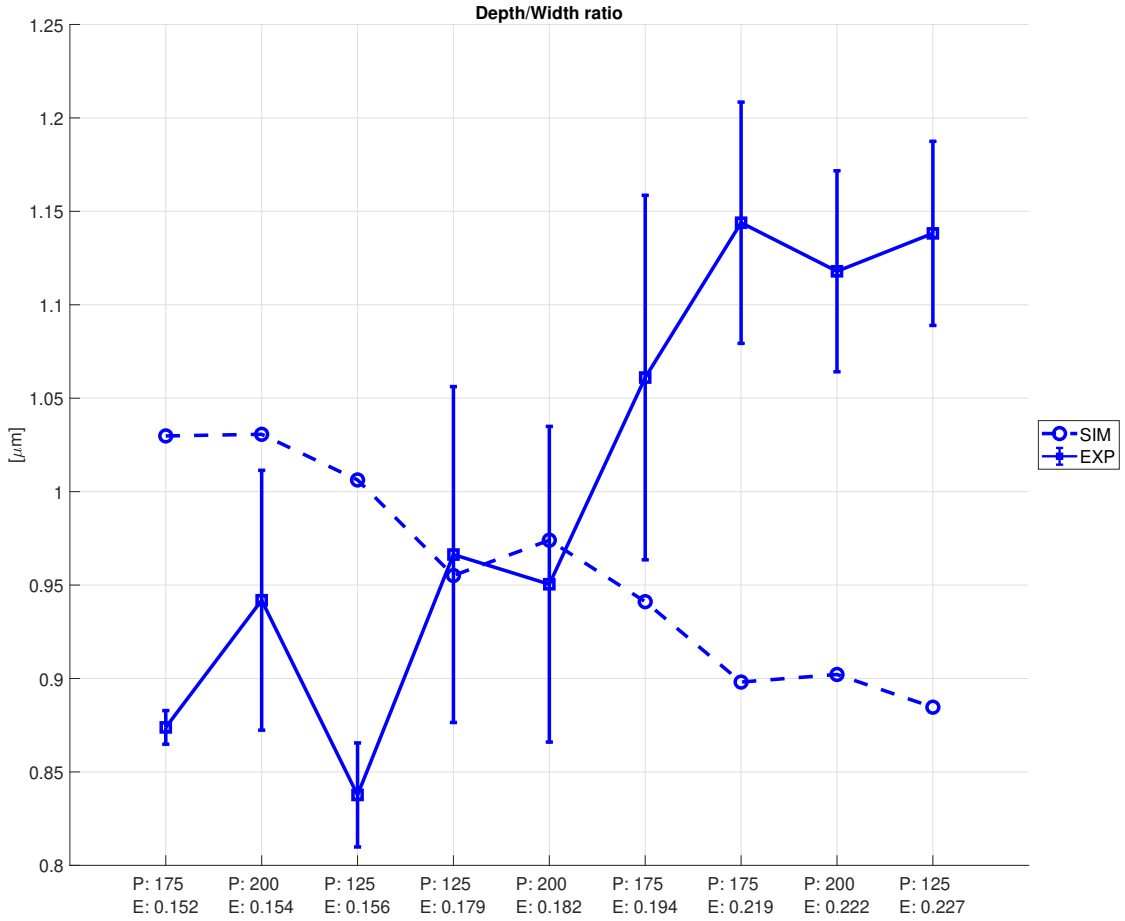

Figure 3.11.: Depth/width-ratio calculated from the simulation results in relation to the experimental result.

The experimental values at the beginning of the track without powder layer are used except in the one condition where the influence of the plume is assumed to make a difference in the experimental outcome which is the condition with P: 125 and E: 0.227. There the value extracted from the end of the track was taken. In Fig. 3.10 one can

a $[mm]$	b $[mm]$	cf $[mm]$	cr $[mm]$	abs $[-]$
0.04	0.149	0.04	0.06	0.75

Table 3.1.: Goldak parameter set constant for all pr. cond. in Fig. 3.10 and 3.11.

see that the area has already a close trend and matches with the experimental area for all printing conditions except the ones in the lowest and the highest scan speed region. This gives the information that in an energetic perspective the simulation is predicting the outcome good. When observing the melt pool depth and width in the two upper plots of Fig. 3.10 the results may be good around the middle LED values but are failing at the higher and the lower ones. The same trend happens in the depth width plot in

Fig. 3.11. To solve this one needs to take a look back at Fig. 3.7-3.9 to see what could be changed to make the simulation more accurate. The need for a big change in depth and slightly lower change in width is needed while the area should remain as it is. For this purpose Goldak parameter b is chosen to adjust the heat source and achieve a better simulation result. On the basis of the behavior of b from the sensitivity part a linear fit was created and used to approximate the simulation outcome in Excel without the need of the computation in Abaqus. With the set of parameters gathered in the spreadsheet approximation the simulation in Abaqus was conducted. This way it was aimed for that b can be chosen in a way so it follows a linear function in dependence of the LED for each condition. Because in the experiment the trend of the melt pool depth is almost linear to the LED and as b represents the penetration depth it also makes sense that it will be dependent on the energy density. The used Goldak parameters are shown in Tab. 3.2 where the corresponding linear function to determine b is the following:

$$b = 0.929 \cdot LED - 0.0164$$

a $[mm]$	b $[mm]$	cf $[mm]$	cr $[mm]$	abs $[-]$	Laser power $[W]$	Scan speed $[\frac{mm}{s}]$
0.04	0.195	0.04	0.06	0.75	125	550
0.04	0.149	0.04	0.06	0.75	125	700
0.04	0.129	0.04	0.06	0.75	125	800
0.04	0.187	0.04	0.06	0.75	175	800
0.04	0.164	0.04	0.06	0.75	175	900
0.04	0.125	0.04	0.06	0.75	175	1150
0.04	0.190	0.04	0.06	0.75	200	900
0.04	0.153	0.04	0.06	0.75	200	1100
0.04	0.127	0.04	0.06	0.75	200	1300

Table 3.2.: Goldak parameters chosen for each condition with b adapted in a way such that a linear function dependent on the LED determines the b for each condition.

In Fig. 3.12 the result of the simulation for this set of parameters is shown as well as the simulation outcome compared to the depth/width-ratio in Fig. 3.13. The change in the area for this set compared to the one constant for all conditions is not significant but as one can see the simulation is predicting the width and depth much closer as before and also the depth/width-ratio is predicted inside the deviation range almost for every condition. While the general trend of the curve is good represented, it still fails in the region with the lowest energy density. There a further change of the parameter b did not deliver a better result but a change in the absorptivity would. So there could be another dependence where the *absorptivity* needs to be adapted according to a different criteria. The larger deviation between experiment and simulation in the lower energy density region led to taking a closer look at the experimental data and the images. There it turns out that the melt pool shape in the experiment starts to slightly change as shown in Fig. 3.14 while in the simulation the melt pool has always a shape close

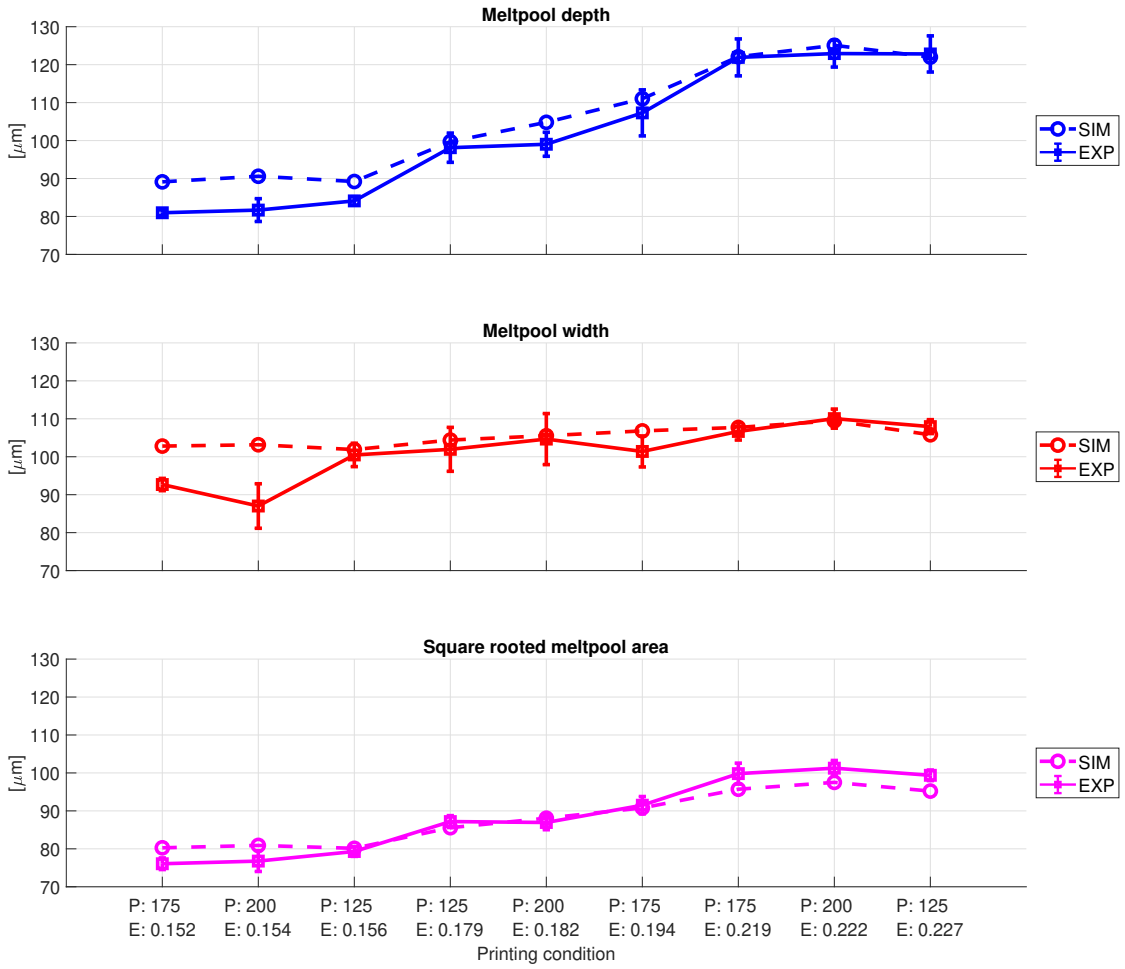

Figure 3.12.: Melt pool dimensions from the simulation compared to the experimental ones with a Goldak b linear dependent of the LED.

to an ellipsoid. In further researches one could examine this phenomenon more specific and find out which parameters make physical sense to be adapted there.

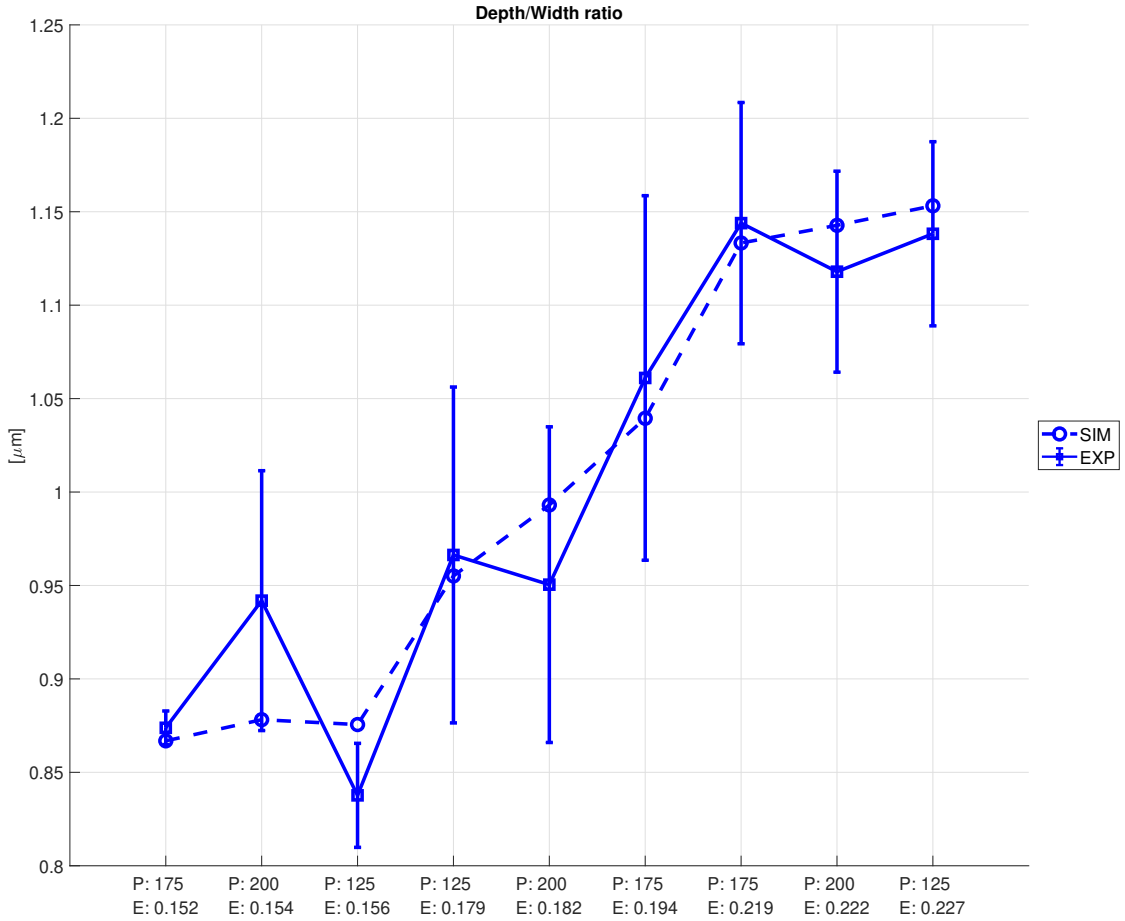

Figure 3.13.: Depth/width-ratio achieved from the simulation with a linear b to the LED in perspective to the experimental ratio.

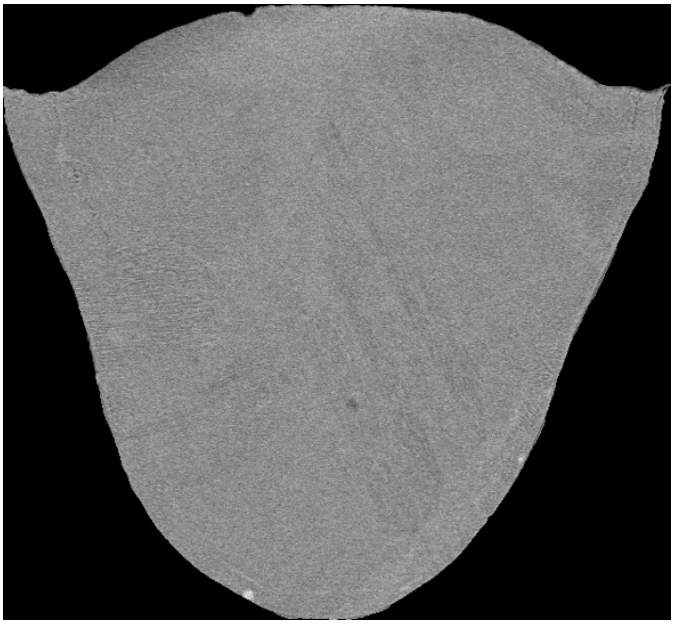

(a) SEM image of the melt pool from one sample of condition P: 125, E: 0.156.

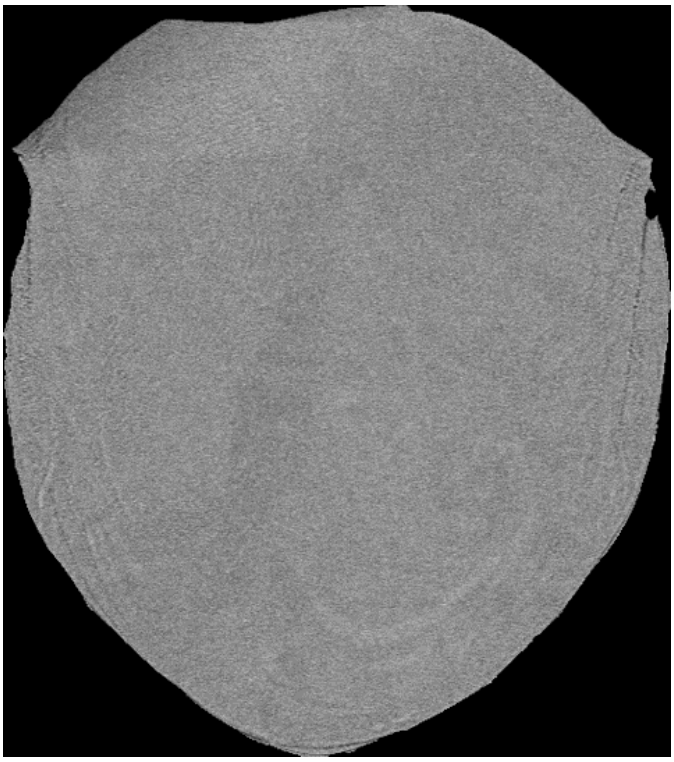

(b) SEM image of the melt pool from one sample of condition P: 200, E: 0.154.

Figure 3.14.: Shape change from left with slower scan speed $800\frac{mm}{s}$ to higher scan speed $1300\frac{mm}{s}$ on the right side.

4. Conclusions

From the experiment one observes that a change in depth is easier achieved by changing scan speed or laser power whereas the width is less sensitive to these printing parameters. The LED seems to have a linear dependence on the depth and can also be used to adjust the depth of the melt pool in a printing job. For the dependence of the printing position the melt pool gets shallower over the printing process while it has an increased width in the end of the track for higher scan speeds and vice versa for lower scan speeds. The uncertainty at the end of the track is in most cases higher than at the beginning. In this case the effect of plume seems to explain this trend. For the behavior of the Simulation parameters the *absorptivity* scales up everything as expected and can be explained thinking about energy input into the system. It is comprehensible that a and b have an effect onto the dimensions aligned to their respective Goldak direction while the dimension perpendicular to them is acting inversely. In the case of Goldak a the sensitivity is lower than the one from b. Compared to the other parameters a change in cf has a negligible effect on the simulated melt pool dimensions, at the same time cr has a slightly decreasing influence on the depth thus also reducing the area as it is also dependent on the width and depth. While cf can be neglected, cr could be used in a case where only a change in depth and area is needed. In the calibration part of the simulation one can see that the Goldak parameters are not constant for all printing conditions. But for a change in b while everything is held constant, the prediction comes very close to the actual results from the experiment as well as it is possible to have b determined by a linear function of the LED. The prediction of the trend suffers the most from the results at high scan speed. These conditions there still have potential for improvement where the linear function of b cannot be used to adapt the simulation to the different printing conditions due to the shape change of the experimental melt pool and the unidentified effect causing this. The heat source parameters can already be determined inside a close range to the experimental values altough the simulation lacks some effects from the real world which cause the high deviation. The prediction is close at the moment but there are still ways for improvement perhaps by adding some of the simpler effects or tuning the heat source parameter even more. For further experiments or projects, it is suggested to keep an eye on the low scan speeds and the plume effect as well as better examine the behavior at very high scan speeds. Especially the shape change of the melt pool could be worth a closer look to explore why this is happening and if there is a physical explanation behind it.

A. Appendix

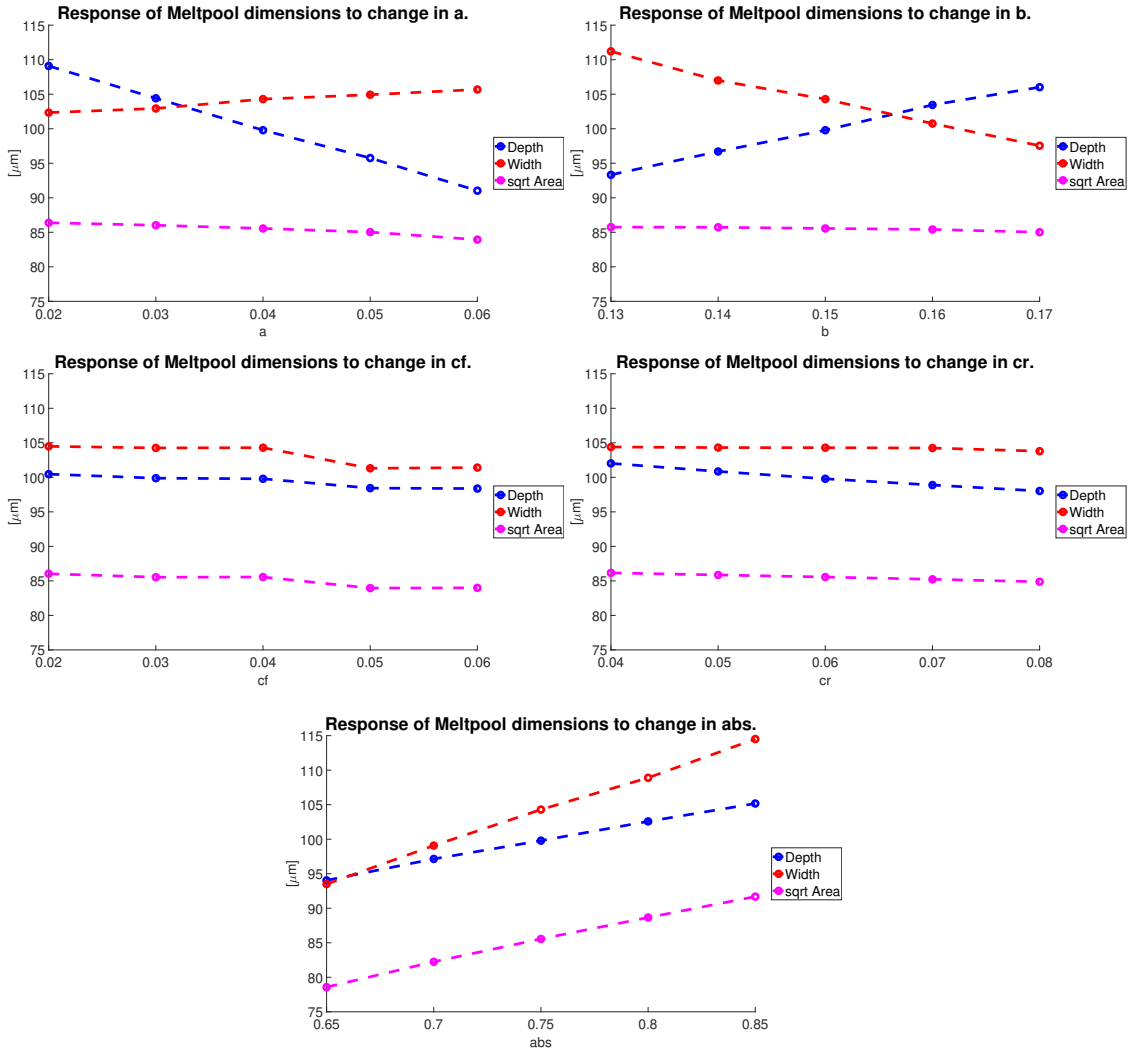

Figure A.2.: The simulation outcome of the melt pool width, depth and square rooted area to a change in each simulation parameter for the printing condition 2 from Tab. 2.1. Only one parameter is changed at a time while the others were held constant with the initial values of $a = 0.04\ mm, b = 0.15\ mm, cf = 0.04\ mm, cr = 0.06\ mm, abs = 0.75$.

Nomenclature

List of Abbreviations

LPBF	$[-]$	Laser Powder Bed Fusion
AM	$[-]$	Additive Manufacturing
MAM	$[-]$	Metal Additive Manufacturing
LED	$[\frac{J}{mm}]$	Line Energy Density
LP	$[W]$	Laser Power
v	$[\frac{mm}{s}]$	Scan Speed
FEM	$[-]$	Finite Element Method

List of Figures

List of Tables

References

[1] Adriano Ambrosi and Martin Pumera. 3D-printing technologies for electrochemical applications. *Chemical Society Reviews*, 45(10):2740–2755, 2016.

[2] Martin Baumers, Phill Dickens, Chris Tuck, and Richard Hague. The cost of additive manufacturing: machine productivity, economies of scale and technology-push. *Technological Forecasting and Social Change*, 102:193–201, 2016.

[3] Maria Madureira Pires. Finite element analysis of residual stresses in metallic parts produced byadditive manufacturing. 2021.

[4] Valeriya Griffiths, James P. Scanlan, Murat H. Eres, Antonio Martinez-Sykora, and Phani Chinchapatnam. Cost-driven build orientation and bin packing of parts in Selective Laser Melting (SLM). *European Journal of Operational Research*, 273(1):334–352, 2019.

[5] Arman Khobzi, Farzaneh Farhang Mehr, Steve Cockcroft, Daan Maijer, Swee Leong Sing, and Wai Yee Yeong. The role of block-type support structure design on the thermal field and deformation in components fabricated by Laser Powder Bed Fusion. *Additive Manufacturing*, 51:102644, 2022.

[6] Jyun-Rong Zhuang, Yee-Ting Lee, Wen-Hsin Hsieh, and An-Shik Yang. Determination of melt pool dimensions using DOE-FEM and RSM with process window during SLM of Ti6Al4V powder. *Optics & Laser Technology*, 103:59–76, 2018.

[7] Snehashis Pal, Nenad Gubeljak, Radovan Hudák, Gorazd Lojen, Viktória Rajt'úková, Tomaž Brajlih, and Igor Drstvenšvek. Evolution of the metallurgical properties of Ti-6Al-4V, produced with different laser processing parameters, at constant energy density in selective laser melting. *Results in Physics*, 17:103186, 2020.

[8] Dassault Systemes. SIMULIA User Assistance. 2021.

[9] Inc. Haynes International. HASTELLOY® X ALLOY. 1997.

[10] Ali Keshavarzkermani, Ehsan Marzbanrad, Reza Esmaeilizadeh, Yahya Mahmoodkhani, Usman Ali, Pablo D. Enrique, Norman Y. Zhou, Ali Bonakdar, and Ehsan Toyserkani. An investigation into the effect of process parameters on melt pool geometry, cell spacing, and grain refinement during laser powder bed fusion. *Optics & Laser Technology*, 116:83–91, 2019.

[11] K. Q. Le, C. Tang, and C. H. Wong. On the study of keyhole-mode melting in selective laser melting process. *International Journal of Thermal Sciences*, 145:105992, 2019.

[12] Christian Tenbrock, Tobias Kelliger, Niklas Praetzsch, Marcel Ronge, Lucas Jauer, and Johannes Henrich Schleifenbaum. Effect of laser-plume interaction on part quality in multi-scanner Laser Powder Bed Fusion. *Additive Manufacturing*, 38:101810, 2021.

[13] Hang Zheng, Huaixue Li, Lihui Lang, Shuili Gong, and Yulong Ge. Effects of scan speed on vapor plume behavior and spatter generation in laser powder bed fusion additive manufacturing. *Journal of Manufacturing Processes*, 36:60–67, 2018.

[14] Jeff E. Irwin, Qian Wang, Panagiotis (Pan) Michaleris, Abdalla R. Nassar, Yong Ren, and Christopher B. Stutzman. Iterative simulation-based techniques for control of laser powder bed fusion additive manufacturing. *Additive Manufacturing*, 46:102078, 2021.

Eidgenössische Technische Hochschule Zürich
Swiss Federal Institute of Technology Zurich

Eigenständigkeitserklärung

Die unterzeichnete Eigenständigkeitserklärung ist Bestandteil jeder während des Studiums verfassten Semester-, Bachelor- und Master-Arbeit oder anderen Abschlussarbeit (auch der jeweils elektronischen Version).

Die Dozentinnen und Dozenten können auch für andere bei ihnen verfasste schriftliche Arbeiten eine Eigenständigkeitserklärung verlangen.

Ich bestätige, die vorliegende Arbeit selbständig und in eigenen Worten verfasst zu haben. Davon ausgenommen sind sprachliche und inhaltliche Korrekturvorschläge durch die Betreuer und Betreuerinnen der Arbeit.

Titel der Arbeit (in Druckschrift):

Experimental and numerical sensitivity analysis of melt pool dimensions for LPBF Hastelloy X

Verfasst von (in Druckschrift):
Bei Gruppenarbeiten sind die Namen aller Verfasserinnen und Verfasser erforderlich.

Name(n):	**Vorname(n):**
Gächter	Willy

Ich bestätige mit meiner Unterschrift:

- Ich habe keine im Merkblatt „Zitier-Knigge“ beschriebene Form des Plagiats begangen.
- Ich habe alle Methoden, Daten und Arbeitsabläufe wahrheitsgetreu dokumentiert.
- Ich habe keine Daten manipuliert.
- Ich habe alle Personen erwähnt, welche die Arbeit wesentlich unterstützt haben.

Ich nehme zur Kenntnis, dass die Arbeit mit elektronischen Hilfsmitteln auf Plagiate überprüft werden kann.

Ort, Datum	**Unterschrift(en)**
01.07.2022	

Bei Gruppenarbeiten sind die Namen aller Verfasserinnen und Verfasser erforderlich. Durch die Unterschriften bürgen sie gemeinsam für den gesamten Inhalt dieser schriftlichen Arbeit.